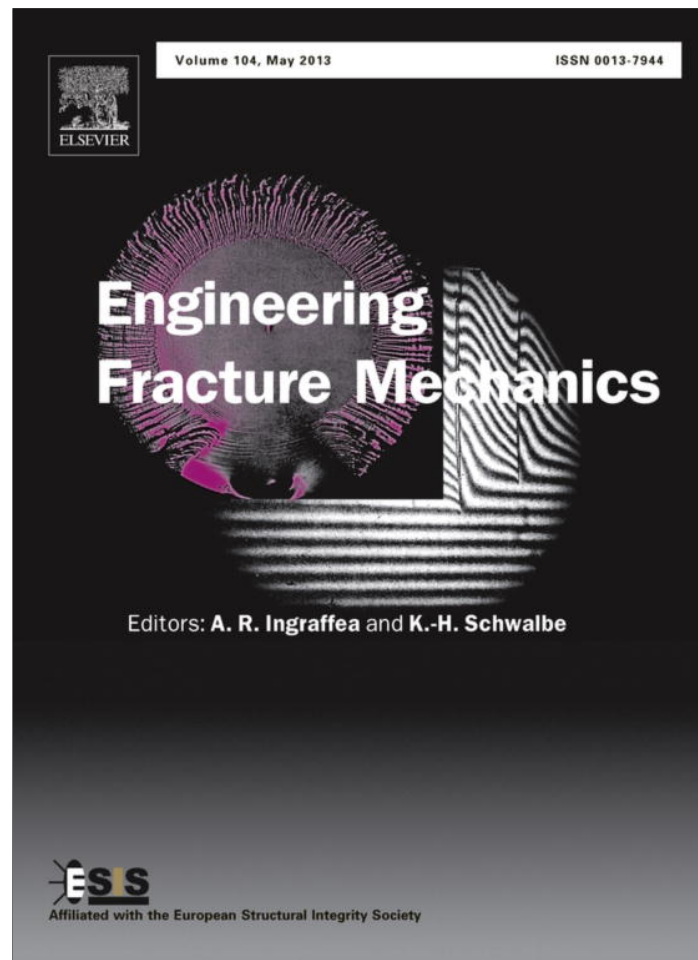


Provided for non-commercial research and education use.
Not for reproduction, distribution or commercial use.



This article appeared in a journal published by Elsevier. The attached copy is furnished to the author for internal non-commercial research and education use, including for instruction at the authors institution and sharing with colleagues.

Other uses, including reproduction and distribution, or selling or licensing copies, or posting to personal, institutional or third party websites are prohibited.

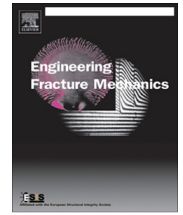
In most cases authors are permitted to post their version of the article (e.g. in Word or Tex form) to their personal website or institutional repository. Authors requiring further information regarding Elsevier's archiving and manuscript policies are encouraged to visit:

<http://www.elsevier.com/authorsrights>



Contents lists available at SciVerse ScienceDirect

Engineering Fracture Mechanics

journal homepage: www.elsevier.com/locate/engfracmech

Modeling flat to slant fracture transition using the computational cell methodology

J. Besson^{a,*}, C.N. McCowan^b, E.S. Drexler^b^a Centre des Matériaux, Mines Paristech, CNRS UMR 7633, BP 87, 91003 Evry Cedex, France^b NIST, Materials Reliability Division (853), 325 Broadway, Boulder, CO 80305, USA

ARTICLE INFO

Article history:

Received 18 September 2012

Received in revised form 19 February 2013

Accepted 23 February 2013

Available online 13 March 2013

Keywords:

Ductile rupture

CTOA specimen

Slant fracture

X100 steel

ABSTRACT

Macroscopic mode I ductile crack propagation in metallic sheets or plates often starts in mode I as a flat triangle (coplanar with the precrack) whose normal corresponds to the loading direction. After some limited extension, the crack becomes slanted and propagates under local mixed mode I/III. Modeling and understanding this phenomenon is challenging. In this work, the “computational cell” methodology proposed in [1], which uses a predefined crack path, is used to study flat to slant fracture transition. The energy dissipation rate is studied as a function of the assumed crack tilt angle. It is shown that a minimum is always reached for an angle equal to 45°. This correlates well with the variation of the crack tip opening angle (CTOA) or the mean plastic deformation along the crack path. Stress and strain states in the stable tearing region hardly depend on the assumed tilt angle. A parametric study shows that flat to slant fracture transition is less likely to occur in materials having high work hardening and favored if additional damage is caused by the local stress/strain state (plane strain, low Lode parameter) in the stable tearing region.

© 2013 Elsevier Ltd. All rights reserved.

1. Introduction

Ductile crack extension in sheet/plates specimens often starts with an initially flat crack coplanar with the precrack which becomes slanted as soon as maximum crack extension is about 1 to 2 times larger than the sheet thickness. This phenomenon was often observed in aluminum alloys [2–6] and steels [7,8]. Pure flat fracture was observed in Al6082 alloy in O temper [9] which has a high hardening capability. Similar results were reported by Pardo et al. [10] on various materials having a high hardening capacity. In the case of large plates made of grade X70 pipeline steel [8] it was found that flat fracture occurred under quasi-static loading conditions whereas slant fracture was observed for dynamic loading. This was interpreted as an effect of adiabatic heating which lowers the hardening capacity thus promoting slant fracture. In higher grades with a lower work hardening, such as X100, slant fracture is always observed unless significant delamination occurs [11]. These results clearly show that slant fracture is promoted in materials with low hardening capacity.

Modeling the flat to slant transition using continuum damage mechanics remains a difficult task in particular if the crack path is not prescribed. In 2D plane strain or axisymmetric cases, crack path changes and slant fracture were simulated using continuum damage mechanics using the Gurson [12] model and its extensions. Axisymmetric cup-cone fracture was successfully simulated [13,14] as well as plane strain slant fracture [15]. This method was recently extended [16,17] by introducing discontinuities based on a bifurcation analysis. Note that cup-cone fracture was also reproduced using a cohesive zone model [18].

* Corresponding author.

E-mail address: jacques.besson@mines-paristech.fr (J. Besson).

Nomenclature

A_n, A_{n2}	damage nucleation rate, secondary nucleation rate
\underline{E}	Green–Lagrange strain tensor
B	sheet thickness
CTOA	crack tip opening angle
E, ν	Young's modulus, Poisson's ratio
f, f_n, f_{n2}, f_t	porosity due to void growth, porosity due to nucleation, porosity due to secondary nucleation, total porosity
F	force
H, b, α	parameters describing flat to slant transition
q_1, q_2, f_*, f_c, f_R	GTN model parameters
p	cumulated plastic strain
R	energy dissipation rate
\underline{s}	stress tensor deviator
U	dissipated energy
Δa	crack advance
$\dot{\epsilon}_0, \sigma_0, n$	model parameters describing rate dependence
$\underline{\epsilon}_p$	plastic strain tensor
Λ	Lode invariant of the stress tensor
Φ	yield surface
$\underline{\sigma}$	Cauchy stress tensor
σ_{eq}	von Mises stress
σ_{kk}	trace of the stress tensor
σ_*	effective stress measure
σ_f	flow stress
σ_N, N	power law hardening parameters
τ	stress triaxiality ratio
θ_0, θ	initial, final tilt angle

The actual flat to slant transition is a fully 3D problem which was first addressed by Mathur et al. [19] in the case of dynamic crack growth but no attempt was made to compare results with actual tests. The transition was also modeled by Besson et al. [20] but simultaneously matching crack paths and load–displacement curves was not possible. The flat to slant transition was obtained using an explicit simulation by Xu and Wierzbicki [21,22] but comparison with experiments was missing. The authors used a damage growth law depending on the Lode parameter of the stress tensor to favor slant fracture. More recently the flat to slant transition was reproduced using an implicit simulation algorithm in [23] using strain controlled damage nucleation depending on the Lode parameter of the strain rate tensor; a satisfactory comparison with experiment was obtained. The main problem encountered while performing such FE simulations, is that a large number of elements must be introduced to allow for crack path change from flat to slant. The number of elements (as well as the model parameters) influences the result of the simulation and it was shown that using too few elements leads to flat crack growth [20,14,22]. This can be partially attributed to the mesh size dependence observed in the case of strain softening materials.

In order to solve the problem of crack path dependence within the continuum damage mechanics approach, it is possible to use the so called “computational cell” technique proposed by Xia et al. [24,1]. Following this method, ductile fracture is confined to a material layer ahead of the initial crack. The layer's thickness is prescribed as a model parameter. It is modeled by a single row of uniformly sized cells represented by one single finite element. The material outside of this strip remains undamaged. The method was first used for 2D plane strain problems and rapidly extended to 3D cases [25–28]. An alternative approach consists in using cohesive zone models. It is however known that the stress triaxiality dependence which is characteristic of ductile fracture is not well captured by such models so that cohesive parameters should depend on the local stress state [29].

In this work the “computational cell” methodology is used to simulate flat to slant transition in a grade X100 line pipe steel. A slanted crack path is meshed using different tilt angles. Local strain and stress states as well as macroscopic quantities such as the energy dissipation rate, the crack tip opening angle (CTOA), crack front shape and area reduction are studied as function of the tilt angle. The numerical tool is then used to study the effect of work hardening and secondary void nucleation.

2. Material and testing procedure

2.1. Material and tensile properties

The material of this study is an X100 grade high strength steel. Such materials are elaborated using thermomechanically controlled rolling and accelerated cooling (TMCP process). It was supplied as a 20 mm thick pipe which was produced by the

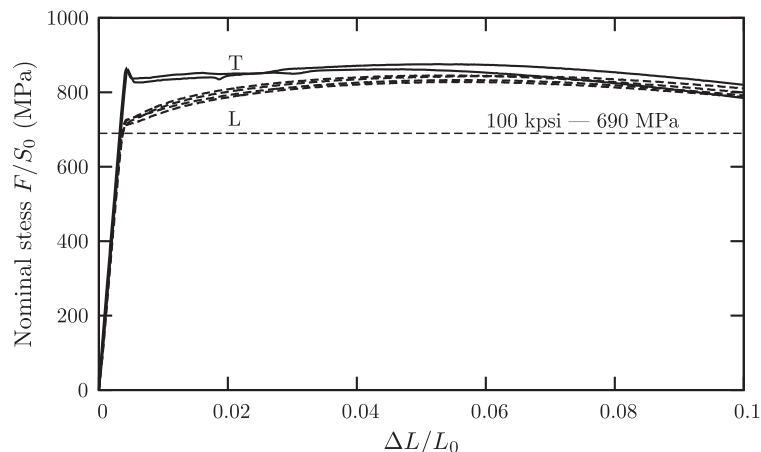


Fig. 1. Tensile curves (engineering stress vs. engineering strain) for *T* (solid lines) and *L* (dashed lines) loading directions (F : force, S_0 : initial cross-section, ΔL : gage length variation, L_0 : initial gage length).

UOE process.¹ The pipe outer diameter was 1.22 m. The microstructure of the dual phase X100 contains mostly ferrite and bainite. Due to material processing, the initial plate has an anisotropic plastic behavior so that it is important to keep track of the material principal axes. In the following the longitudinal direction corresponding to the rolling direction (or pipe axis) is referred to as *L*; the transverse direction is referred to as *T*. During UOE forming, the material is prestrained along the *T* direction which corresponds to the hoop direction of the pipe. The yield stress of the material along the *T* direction should be larger than 690 MPa (or 100 kpsi) after UOE forming to obtain X100 grade product.

Tensile tests were carried out along the *L* and *T* directions using a nominal strain rate equal to 10^{-3} s^{-1} . The initial specimen diameter is equal to 12.7 mm ($\frac{1}{2}$ in). This diameter is close to the pipe thickness so that the test is representative of an “average material” as gradients (in particular prestrain gradients) may exist through the pipe wall thickness [30]. Results are shown in Fig. 1 where the engineering stress is plotted as a function of the engineering strain. The *T* direction exhibits a higher yield stress and a lower work-hardening rate. These results are consistent with the fact that the material was prestrained along the *T* direction during forming. This can be described using kinematic hardening as shown by Shinohara et al. [31]. Additional differences between *T* and *L* loading may originate from the anisotropic texture of the material [31,32]. Tensile tests along the *T* direction present an upper yield which will be neglected in the simulations.

2.2. Testing of CTOA specimens

Large crack extension tests involving both crack initiation and crack propagation were carried out using modified double cantilever beam (MDCB) (see Darcis et al. [33]). The specimen dimensions are depicted in Fig. 2. Test specimens were extracted from curved plates cut from the longitudinal axis of the pipe so that tests were carried out in the *T*–*L* orientation. The thickness of each curved plate was reduced by machining to obtain a flat plate. Its thickness is 8 mm. Due to the pipe curvature, the actual test section is between approximately $0.25t$ and $0.67t$ measured from the internal diameter, where t is the pipe thickness. The loading of the specimen was conducted using a pair of 10 mm thick plate grips (17–4 ph stainless steel) bolted to the side surfaces of the specimen, using eight holes (Fig. 2). The eight holes facilitate a uniform load transfer between the specimen and the plate grips. Two common macroscopic steady-state fracture profiles that occur on slanted fracture planes are addressed here: V-shaped and S-shaped. The V-shape fracture (or roof top) occurs on two slanted planes and the intersection of the slant planes forms a V-shape. The S-shaped fractures occur on a single slanted plane, but slight curves near the free surfaces of the cross sections form an S-shaped profile.

Typical force–displacement curves are plotted in Fig. 3b showing a good reproducibility. The macroscopic fracture pattern is also shown in Fig. 3a. As mentioned above, cracking initiates within a flat triangular region. In the case shown here, a V-shape (or roof top) fracture is then observed followed by a S-shape region. In other cases, pure S-shape fracture was observed but the fracture mode had no discernible effect on the force–displacement curve. The crack tilt angle is about 45° in these two regions. The fracture surface shows large ductile dimples in the flat triangular region. In the propagation zone, reverse chevron markings are formed by primarily ductile fracture features, but some isolated regions of quasi-cleavage are present on the fracture surfaces. The detailed description of the fracture surfaces is given in [34].

The CTOA was measured using the method proposed in Darcis et al. [33]; measured values are $8.5^\circ \pm 2$. A grid was painted (via a laser process) on the gage section of the specimens prior to testing. A grid was painted (via a laser process) on the gage section of the specimens prior to testing that was 20 mm wide (loading direction) and 80 mm long (crack propagating direction). The elongation measured perpendicular to the direction of crack propagation over a the 20 mm gage width outside of the initiation region is about 19% (engineering strain). The elongation is close to 0 (i.e. plane strain) along the crack propa-

¹ UOE forming is a manufacturing process where the plate material is first deformed into an U-shape then an O-shape. The pipe seam is then welded. The pipe is finally expanded using an internal mandrel. To achieve low ovality, the pipe is typically expanded by 0.8–1.3% from its diameter after the O-step [30].

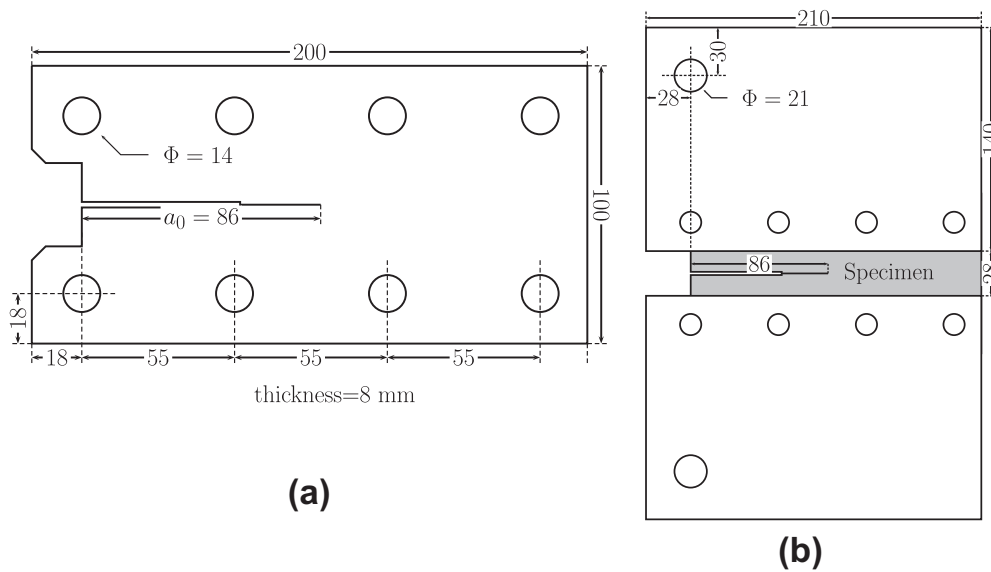


Fig. 2. (a) MDCB specimen and (b) plate grip, configuration and dimensions (in mm).

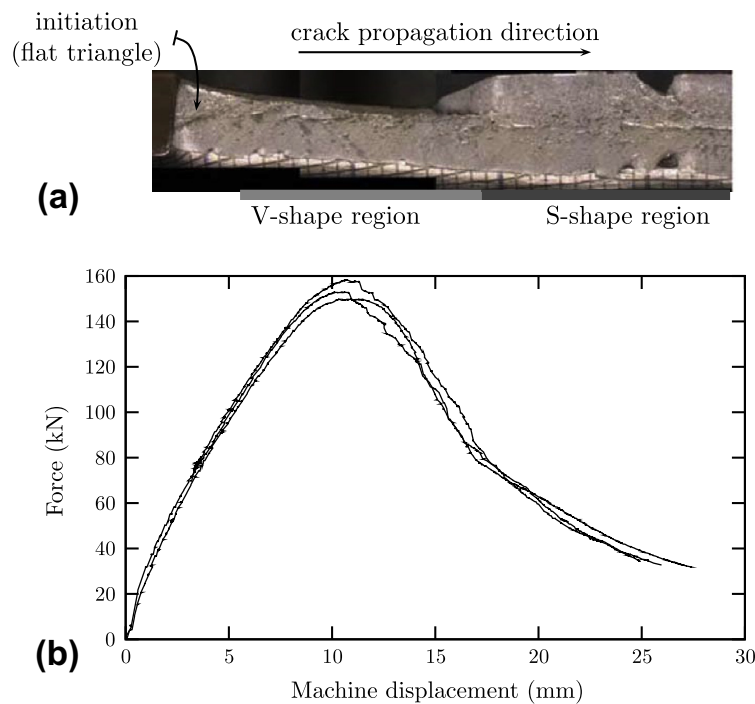


Fig. 3. (a) Macroscopic aspects of ductile tearing showing a flat initiation triangle, which transitions into a zone of V-shaped slant fracture (V-shape with point of the V up and off-centered, in this example, \wedge , like a roof top), followed by a zone having an S-shape slant fracture with a ridge, which is visible at the centerline of the pipe. (b) Force vs stroke curves for MDCB specimens.

gation direction. In some cases double grids (front and back) were laid on the specimens to gain information on the tilt of the fracture plane in reference to the “non-deformed” specimen. The angles measured using the two grids ranged between 27° and 37°.

3. Material modeling and simulation technique

3.1. Constitutive equations for ductile damage growth

Despite the fact that the material is known to have an anisotropic plastic behavior [32] together with mixed isotropic/kinematic hardening [31], plastic isotropy and isotropic hardening will be assumed in the following for the sake of simplicity. In the following, the Gurson–Tvergaard–Needleman (GTN) model [12,35] is used to describe the strong coupling between

plastic deformation and damage growth. Following the computational cell methodology, the GTN will only be used within the fine strip where damage can grow. Standard plastic behavior is used outside of this zone. In the strip, the material is assumed to contain initial voids (volume fraction f_0). An effective stress measure (σ_*) which simultaneously accounts for the macroscopic stress tensor ($\underline{\sigma}$) and damage (f_t which represents the sum of the void volume fraction, f , and the nucleated damage, f_n) is implicitly defined by the following equation:

$$\frac{\sigma_{eq}^2}{\sigma_*^2} + 2q_1 f_* \cosh\left(\frac{q_2}{2} \frac{\sigma_{kk}}{\sigma_*}\right) - 1 - q_1^2 f_*^2 \stackrel{\text{def.}\sigma_*}{=} 0 \quad (1)$$

where σ_{eq} is the von Mises equivalent stress, σ_{kk} the trace of the stress tensor. f_* is a function of the actual total porosity f_t introduced by Tvergaard and Needleman [13] to simply represent final failure by coalescence:

$$f_* = \begin{cases} f_t & \text{if } f_t < f_c \\ f_c + \left(\frac{1}{q_1} - f_c\right) \frac{f_t - f_c}{f_R - f_c} & \text{otherwise} \end{cases} \quad (2)$$

f_c represent the porosity at which coalescence starts and f_R the porosity level at failure (in that case $f_* = 1/q_1$). q_1 and q_2 are model parameters. The yield function is then expressed as:

$$\Phi = \sigma_* - \sigma_f(p) \quad (3)$$

where σ_f is the flow stress of the undamaged material and p the cumulated plastic strain. The plastic strain rate tensor is obtained using the normality rule

$$\dot{\epsilon}_p = (1 - f) \dot{p} \frac{\partial \Phi}{\partial \underline{\sigma}} = (1 - f) \dot{p} \frac{\partial \sigma_*}{\partial \underline{\sigma}} \quad (4)$$

The plastic strain rate, \dot{p} , is obtained assuming that the material is slightly rate-dependent as:

$$\dot{p} = \dot{\epsilon}_0 \langle \Phi / \sigma_0 \rangle^n \quad (5)$$

where $\dot{\epsilon}_0$, σ_0 and n are model parameters. Note that the cumulated plastic strain is such that: $\sigma_* \dot{p} = (1 - f) \underline{\sigma} : \dot{\epsilon}_p = (1 - f) \sum_{ij} \sigma_{ij} \dot{\epsilon}_{p_{ij}}$. Following Chu and Needleman [36] damage growth is expressed as:

$$\dot{f}_t = \dot{f} + \dot{f}_n = (1 - f_t) \text{trace}(\dot{\epsilon}_p) + A_n \dot{p} \quad (6)$$

where $\dot{f} = (1 - f_t) \text{trace}(\dot{\epsilon}_p)$ represents void growth and $\dot{f}_n = A_n \dot{p}$ represents strain controlled nucleation. A_n is a material parameter which needs to be adjusted. It represents the damage nucleation rate.

The isotropic hardening function $\sigma_f(p)$ was fitted considering tensile tests along the T direction (see Fig. 1) as CTOA tests are performed with the loading direction corresponding to the T direction. Damage parameters were taken equal to those previously used to describe ductile damage and failure of a similar material by Tanguy et al. [32]. Parameters were fitted using tests on smooth and notched axisymmetric bars. All model parameters are gathered in Table 1.

The above constitutive equations were implemented into the “in-house” finite element code Zset [37,38] using a fully implicit time integration scheme. As ductile rupture is always accompanied by large deformations, a finite strain formalism must be used. In this work the treatment of finite strain is based on the use of a reference frame which allows keeping a standard additive strain rate decomposition [39]. A co-rotational reference frame attached to the material is defined by the rotation tensor \underline{Q}_c . Its evolution law is given by:

$$\dot{\underline{Q}}_c = \underline{\underline{\Omega}} \cdot \underline{Q}_c \quad \text{with} \quad \underline{Q}_c(t=0) = \underline{1} \quad (7)$$

\underline{D} and $\underline{\underline{\Omega}}$ are the symmetric and skew-symmetric parts of the velocity gradient. The rotated stress and strain rate tensors ($\underline{\underline{\sigma}}$ and $\underline{\underline{\dot{\epsilon}}}$) are obtained by transport of the Cauchy stress ($\underline{\underline{\Sigma}}$) and the deformation rate (\underline{D}) tensors into the co-rotational reference frame as: $\underline{\underline{\sigma}} = \underline{Q}_c \cdot \underline{\underline{\Sigma}} \cdot \underline{Q}_c^T$ and $\underline{\underline{\dot{\epsilon}}} = \underline{Q}_c \cdot \underline{D} \cdot \underline{Q}_c^T$. The corresponding objective stress rate is the Jauman rate.

Table 1
Material model parameters.

Elastic properties	$E = 210 \text{ GPa}$, $\nu = 0.3$
Plastic hardening	$\sigma_f(p) = 835 \left(\frac{p+0.01}{0.01}\right)^{0.05} \text{ (MPa)}$
Strain rate effect	$\sigma_0 = 55 \text{ MPa}$, $\dot{\epsilon}_0 = 1 \text{ s}^{-1}$, $n = 5$
GTN model	Initial damage $f_0 = 1.35 \times 10^{-4}$ $q_1 = 1.6$, $q_2 = 1$, $f_c = 0.02$, $f_R = 0.15$ $A_n = 0.02$ for $0.5 \leq p \leq 1.0$ and $A_n = 0$ otherwise

3.2. Numerical procedures for the finite element simulations

Finite element calculations were performed using 8-node finite strain bricks using selective integration [40]. To simplify simulation, the detailed experimental setup (i.e. plate grips, holes, bolts. . .) is replaced by a thicker plate (thickness: 15 mm) directly attached to the specimen. Fillets (diameter: 5 mm) are used to generate a gradual transition between the sample (thickness: 8 mm, height: 28 mm) and the loading plates. Following the computational cell methodology Xia and Shih [1], the process of ductile fracture is confined to a material layer of initial thickness h ahead of the initial crack. The transition zone between flat and slant fracture is meshed using the following parametrization of the fracture surface where x , y and z denote the position along the crack extension direction, the loading direction and the thickness direction:

$$\begin{aligned}
 \text{zone } \textcircled{1} \quad & y = 0 \\
 \text{zone } \textcircled{2} \quad & y = \tan(\theta_0) \sin\left(\frac{\pi}{2} \frac{x}{H}\right) \frac{z}{|z|} \left(|z|^n - \left(\frac{b}{2}\right)^\alpha \left(1 - \frac{x}{H}\right)^n \right)^{\frac{1}{2}} \\
 \text{zone } \textcircled{3} \quad & y = \tan(\theta_0)z
 \end{aligned} \tag{8}$$

Zone ① corresponds to the flat triangle where cracking starts; zone ③ corresponds to the slanted crack path characterized by the initial tilt angle θ_0 and ② to the transition zone (see Fig. 4). The parametrization of zone ② (with $\alpha = 2$) is so as to obtain a continuous smooth transition with the other two zones. The resulting mesh is shown in Fig. 5a. A detailed view of the crack propagation area is shown in Fig. 5b/c. The computational cell methodology allows forcing a slant fracture path (S-shape and V-shape).

The crack propagation zone has a total length of 24.8 mm. Twelve elements are used along the thickness direction. The element height is $h = 0.2$ mm; the element length along the crack propagation direction is also equal to 0.2 mm. The total number of elements along the crack path is therefore equal to 1488. The 3D crack path is shown in Fig. 5c. The mesh contains 32,200 elements. When the material is considered as broken at eight Gauss points within an element, the element is removed from the calculation. To avoid getting a singular global stiffness matrix, displacement increments of nodes belonging only to removed elements are then prescribed to 0. Different meshes were generated using initial tilt angles θ_0 between 0° and 45° . Due to large deformations, the initial crack surface (xz plane) rotates about the x -axis toward the loading direction (y -direction) so that the tilt angle after crack advance, θ , increases. Based on the fracture surface observation, the following dimensions are used: $B = 8$ mm, $b = H = 7$ mm. Additional meshes of half of the structure ($z \geq 0$ only) were also generated. Such meshes allow to represent V-shape fracture as in that case the xy plane is a symmetry plane.

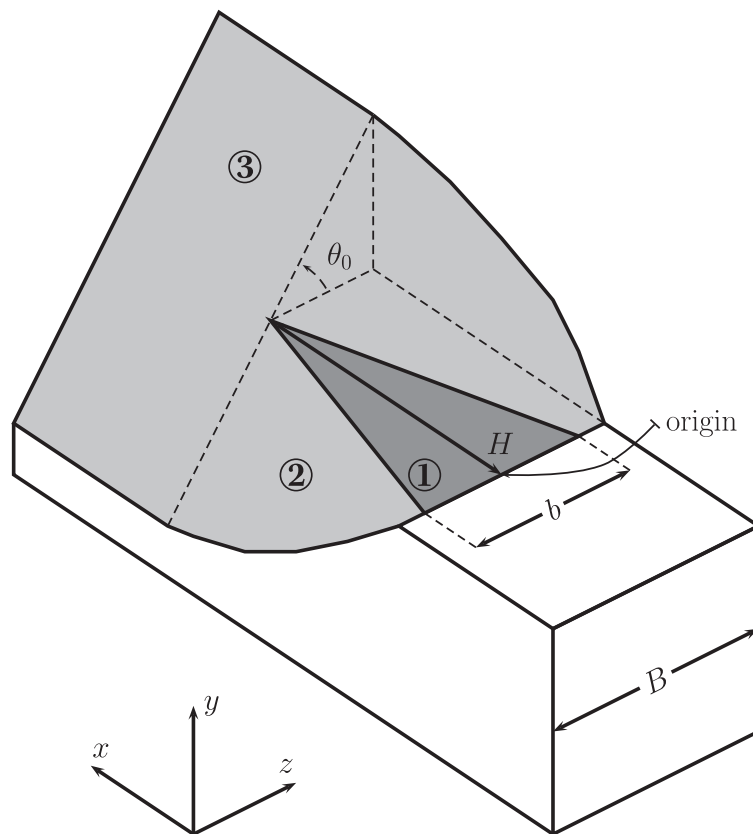


Fig. 4. Schematic representation of the flat to slant transition zone described using Eq. (8).

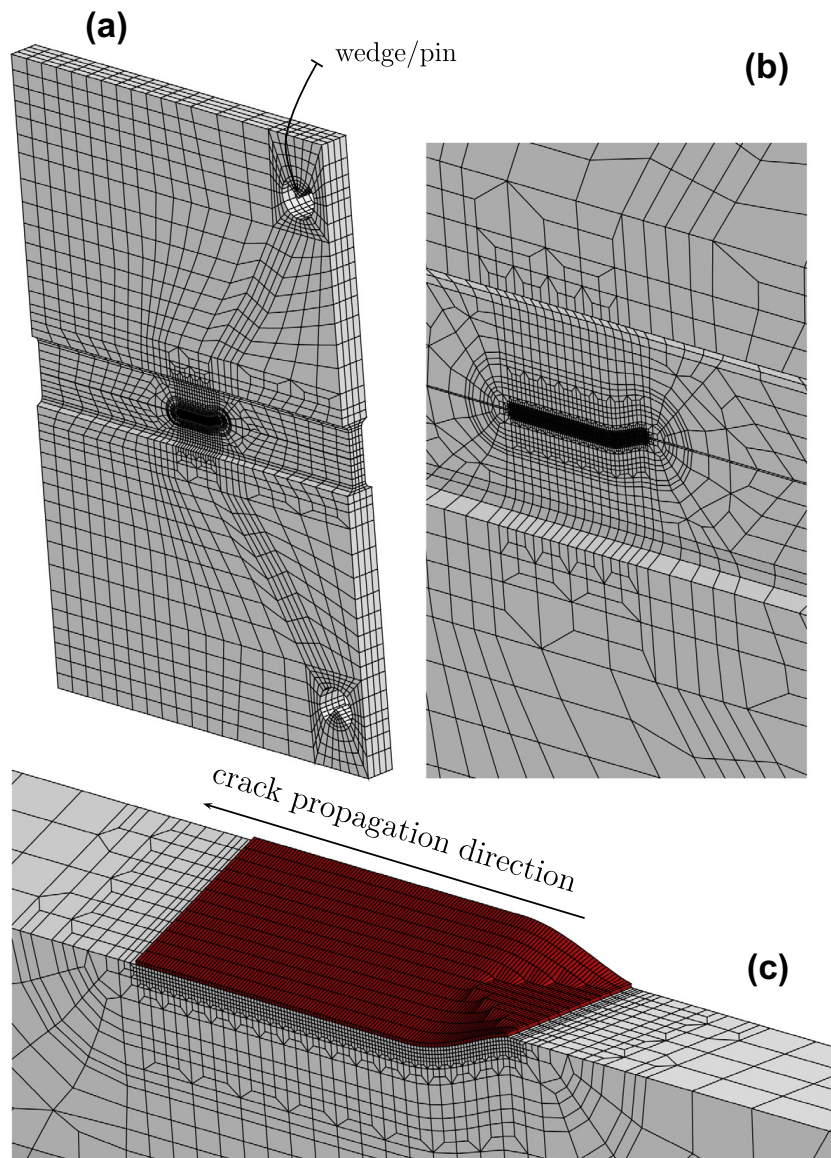


Fig. 5. Finite element mesh of the CTOA specimen: (a) full mesh, (b) detailed view of the crack propagation area, (c) detailed view of the crack propagation area showing the element band, where the crack is allowed to propagate ($\theta_0 = 25^\circ$).

Boundary conditions consist of prescribed displacements applied on the top of the wedges shown in Fig. 5a. The wedges are assumed to remain elastic. In that case S-shape fracture is obtained. In order to simulate V-shape fracture path only half a mesh is required due to symmetry. In that case, displacement along the thickness direction (u_z) are fixed to 0 for nodes in the $z = 0$ plane.

4. Results

4.1. V-shape cracking versus S-shape cracking

Simulations were carried using initial tilt angles between 0° and 45° for S-shape (full meshes) and V-shape (half meshes) fracture paths. Load–displacement curves are shown in Fig. 6. Crack initiation (first element considered as broken) occurs early while the overall behavior is still linear elastic. At load maximum about half of the triangular region is cracked. The load maximum is not affected by the initial tilt angle as cracking is still limited to the flat area at this point. Depending on the tilt angle, different load–displacement curves are obtained. In the case where V-shape fracture is assumed (Fig. 6a) the load for a given imposed displacement continuously increases whereas it first decreases and then increases in the case of S-shape fracture (Fig. 6b). FE simulations were post-processed to evaluate crack advance. The crack tip position with respect to the load-line (determined by the position of the “broken” Gauss points) is evaluated for each row of Gauss points aligned with respect to the crack propagation direction. The crack tip position is averaged along the crack front to obtain the

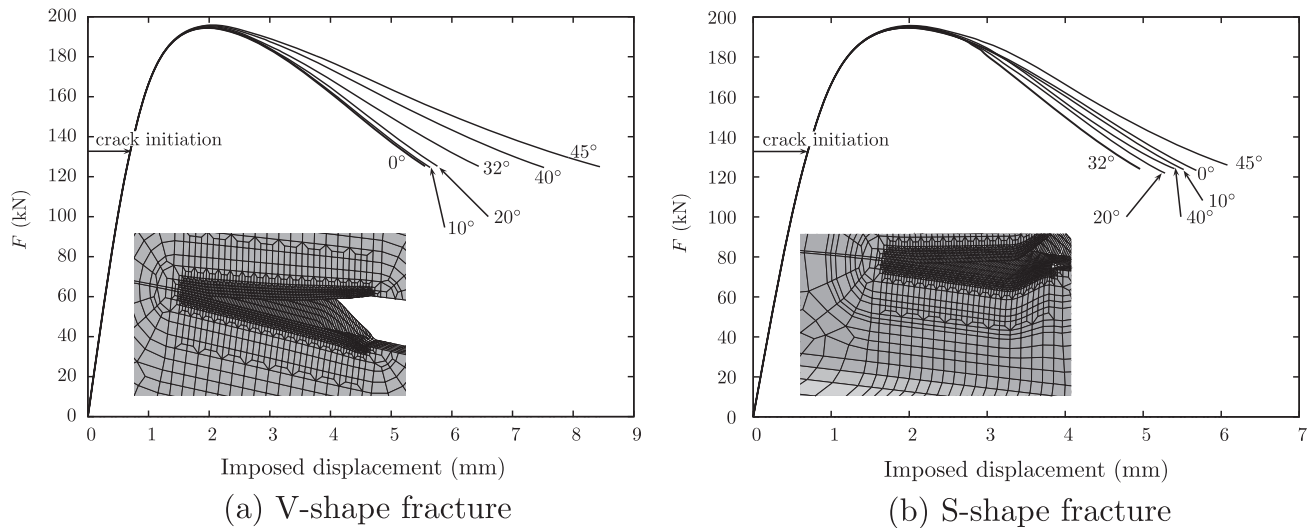


Fig. 6. Force–displacement curves for various initial tilt angles: (a) calculations assuming V-shape fracture (half mesh) and (b) calculations assuming S-shape fracture (full mesh). Deformed meshes ($\theta_0 = 35^\circ$) are also shown to visualize crack advance (broken elements have been removed).

average crack length, a . The crack extension, Δa , is calculated as the difference between crack lengths at different loading steps. S-shape and V-shape cracking occurs under stationary conditions (i.e. same final tilt angle, same local strain and stress state) for crack advances between 7 mm and 17 mm.

Due to large strains, the prescribed crack path tends to rotate towards the loading direction so that the initial tilt angle varies. The final tilt angle is plotted as a function of the initial tilt angle in Fig. 7. In the case of S-shape fracture, θ is computed between both surfaces of the specimens whereas it is computed between the specimen center and the free surface in the case of V-shape fracture. This leads to negative variation of the tilt angle for $\theta_0 = 0$ as shown in Fig. 7.

The energy dissipation rate, R , is evaluated as:

$$R = \frac{1}{B} \frac{\Delta U}{\Delta a} \Big|_{\Delta a=7 \text{ mm} \dots 17 \text{ mm}} \tag{9}$$

where U is the area under force versus displacement curve. R is plotted as a function of the final tilt angle in Fig. 8 for V-shape and S-shape fracture. In Fig. 8 it is shown that R is continuously increasing in the case of V-shape fracture whereas a minimum value is obtained for S-shape fracture. The final tilt angle corresponding to the minimum value of the dissipated energy is very close to 45° which is the actual experimental cracking angle (initial tilt angle equal to 32° in the present case). This result clearly indicates that S-shape slant cracking with an angle close to 45° is the most favorable condition for crack

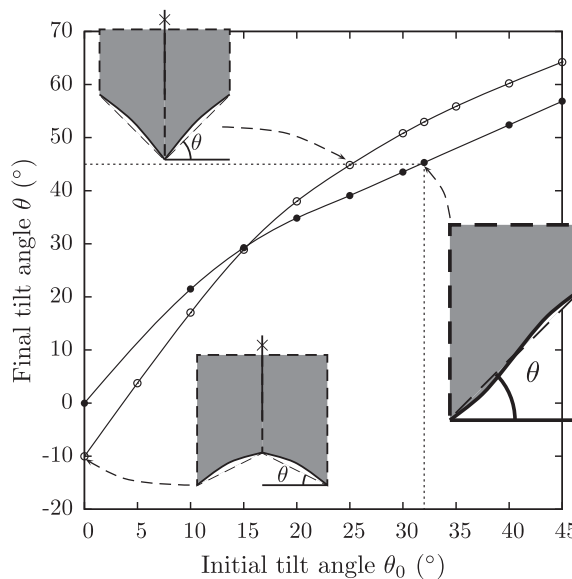


Fig. 7. Final tilt angle θ as a function of the initial tilt angle θ_0 for V-shape fracture (open symbols) and S-shape fracture (closed symbols) CTOA specimens.

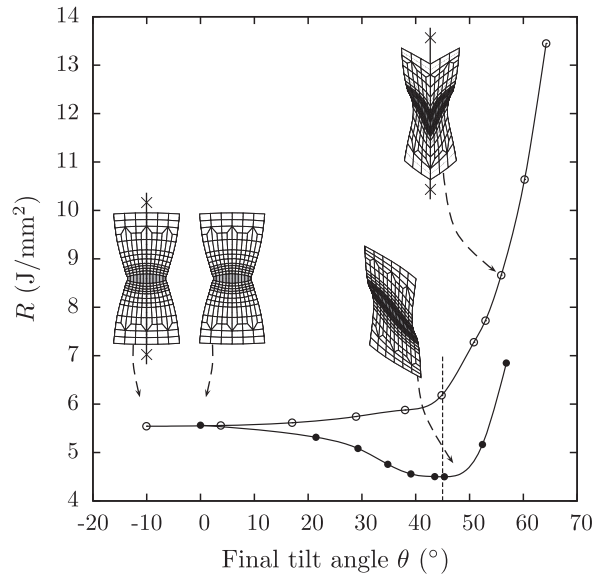


Fig. 8. Energy dissipation rate R as a function of the final tilt angle for V-shape fracture (open symbols) and S-shape fracture (closed symbols) CTOA specimens. Deformed meshes (cross sections perpendicular to the crack advance direction) for $\theta_0 = 0^\circ$ and $\theta_0 = 35^\circ$ are also shown for symmetrized and full specimens. (In the case of V-shape fracture, the full specimen was reconstructed as only half of the specimen is actually computed due to symmetry.)

extension. In the following, calculations will only be performed using a full mesh which is needed to obtain S-shape fracture which is more frequently observed than V-shape fracture.

4.2. Local stress/strain states

In order to understand the reason why R reaches a minimum value for a final tilt angle equal to 45° , local material variables computed at the center of the flat initiation triangle (zone A in Fig. 9), at the center of the slant zone (zone B) and close to the free surface of the slant zone (zone C) were compared. In the following E_{yy} represents the Green–Lagrange strain along the loading direction, E_{xx} the Green–Lagrange strain along the crack propagation direction, τ the stress triaxiality ratio defined as $\frac{1}{3} \sigma_{kk} / \sigma_{eq}$. The last material parameter to be examined is the stress Lode parameter defined as:

$$\Lambda = \frac{27 \det \underline{s}}{2 \sigma_{eq}^3} \quad -1 \leq \Lambda \leq 1 \quad (10)$$

where \underline{s} is the stress deviator. Results are shown in Fig. 9 where solid lines represent data for $\theta_0 = 0^\circ$ and dashed lines data for $\theta_0 = 35^\circ$. It is shown that there are little differences between both calculations in the crack initiation region (which is expected as the crack path is similar) but also in the slanted stationary crack extension region. In addition differences are limited between the center of the specimen (zone B) and the surface (zone C).

Fig. 9a shows the evolution of E_{xx} . In the crack initiation region (A), it rapidly becomes negative but remains close to 0 in the crack propagation region (B and C). This indicates that crack propagation occurs under plane strain conditions (see also [3]). It is however important to notice that the plane strain direction corresponds to the crack advance direction contrarily to the case of thick walled structures where the plane strain direction corresponds to the specimen thickness direction (e.g. as in large Compact Tension specimens). The evolution of damage (f_t) is shown in Fig. 9-b. Damage growth is more rapid in the initiation region than in the propagation region. This is directly related to the stress triaxiality ratio (Fig. 9c) which is higher in zone A than in zones B and C. Similar results were obtained in [41,3,2]. The Lode parameter is shown in Fig. 9d. It is observed that Λ remains close to 0 in the slanted area. This corresponds to the quasi-plane strain state observed in this region as $\dot{\epsilon}_p^{xx} \approx 0$ implies that $s^{xx} \approx 0$ using the normality rule (Eq. 4) so that $\det \underline{s} / \sigma_{eq}^3$ is close to 0.

From the study of the local material variables, no significant differences could be evidenced between flat and slant crack propagation. However, it is shown that crack propagation occurs under plane strain conditions ($E_{xx} \approx 0$ or $\Lambda \approx 0$). Strain localization is easier under plane strain state [42]. In that case, the normal to the localization band lies in the plane normal to the plane strain direction and makes an angle equal to 45° with the loading direction. Consequently the minimum value of the dissipated energy is obtained for the theoretical localization angle which allows confining plastic deformation within a narrow band. This effect can be evidenced by computing the average value of the cumulated plastic strain in a slice of material (shown in Fig. 8) along the crack path. Results are shown in Fig. 10 for V-shape and S-shape fracture. The mean cumulated plastic strain correlates very well with the energy dissipation rate shown in Fig. 8. In particular it reaches a minimum value in the case of S-shape fracture for a final tilt angle equal to 45° .

From these results, it can be concluded that the fact that the energy dissipation rate reaches a minimum value for $\theta = 45^\circ$ is not related to the local stress/strain state along the crack path as it hardly depends on the tilt angle. It is however clearly

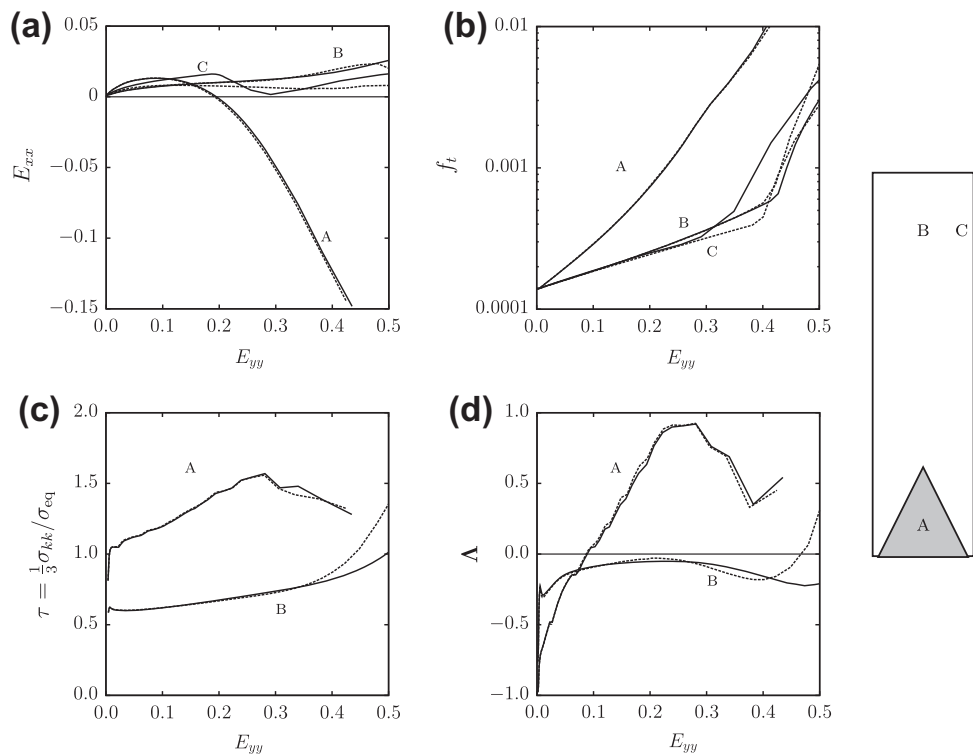


Fig. 9. Local material variables at the center of the flat initiation triangle (zone A, the center of the slant zone (zone B) and close to the free surface of the slant zone (zone C): (a) Green–Lagrange strain along the crack propagation direction (E_{xx}), (b) porosity (f_t), (c) stress triaxiality ratio (τ), and (d) Lode parameter (Λ). Solid lines represent data for $\theta_0 = 0^\circ$ and dashed lines data for $\theta_0 = 35^\circ$. Values at location c are omitted in graphs c and d as they are very close to those calculated for zone b.

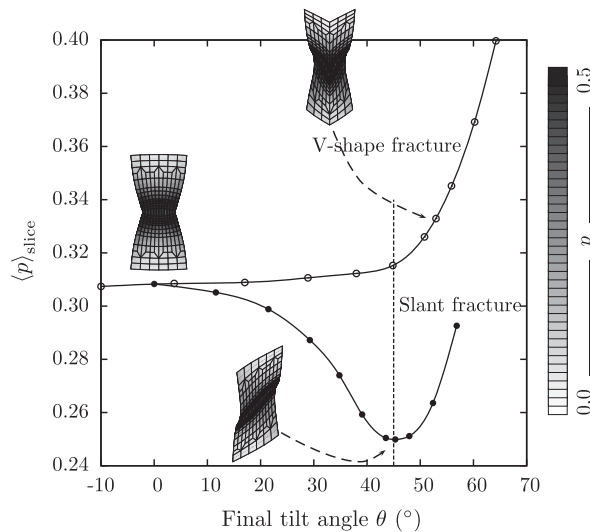


Fig. 10. Mean cumulated plastic strain ($\langle p \rangle_{\text{slice}}$) computed for a slice of material along the crack path (see Fig. 8 as a function of the final tilt angle for full (closed symbols) and half (open symbols) meshes.

related to the plane strain state which favors strain localization. In the case of meshes for which a narrow strain localization and fracture band can be easily formed, plastic deformation along the crack path is minimized: this leads to a lower energy dissipation rate.

4.3. CTOA

Finite element simulations were post-processed to compute the CTOA in the slant region. Due to the discretization, it is not possible to determine the CTOA at the crack tip as in the case of actual experiments [33]. To circumvent the problem,

nodes belonging to broken elements are used to represent the upper and lower crack lips as illustrated in Fig. 11. The upper and lower nodes are used to fit two lines; the CTOA is defined as the angle between these two lines as shown in Fig. 11. 10 elements from the crack tip are used but very little difference is observed using 5 or 15 elements.

Results are shown in Fig. 11 for both V-shape and S-shape fracture. CTOA is computed at the free surface (as in actual tests) but also at the mid-plane. The difference between both sets of results remains small. The evolution of the CTOA as a function of the final tilt angle correlates well with the evolution of the dissipated energy R (Fig. 8) and of the mean plastic strain (Fig. 10). In particular, the CTOA is minimum for a final tilt angle close to 45° for S-shape fracture.

4.4. Crack front shape

It is often observed that the crack front is curved with the crack advance being always longer at the center of the specimens (so called “tunneling effect”) [43]. However, once a stable regime has been reached, the crack advance rate at the center is equal to the crack advance rate at the free surface. It is also observed that the crack front curvature is larger for flat crack propagation than for slant crack propagation. In this study, tunneling was characterized by monitoring the crack front in the steady state crack propagation regime. The crack front projected on the x – z is shown in Fig. 12a for various initial tilt angles. It is shown that tunneling is maximum for $\theta_0 = 0^\circ$ (i.e. flat fracture) and minimum for $\theta_0 = 30^\circ$. The crack front aspect ratio (defined by the depth (d) to width (w) ratio) is also shown on Fig. 12b as a function of the final tilt angle. A minimum value is obtained for θ close to 45° .

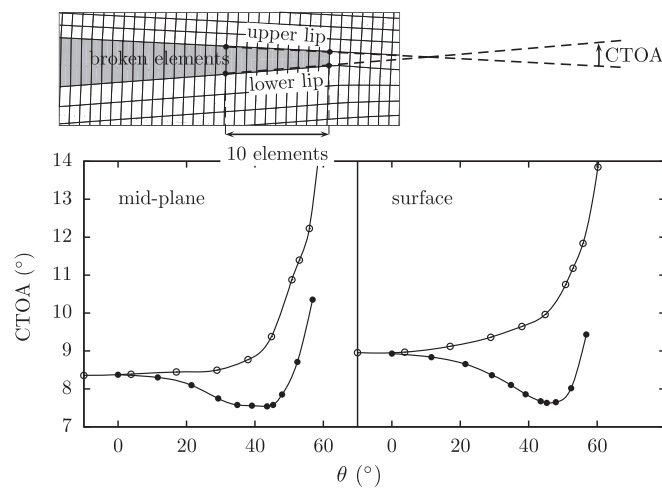


Fig. 11. Evolution of the CTOA as a function of the final tilt angle for V-shape (open symbols) and S-shape (closed symbols) fracture.

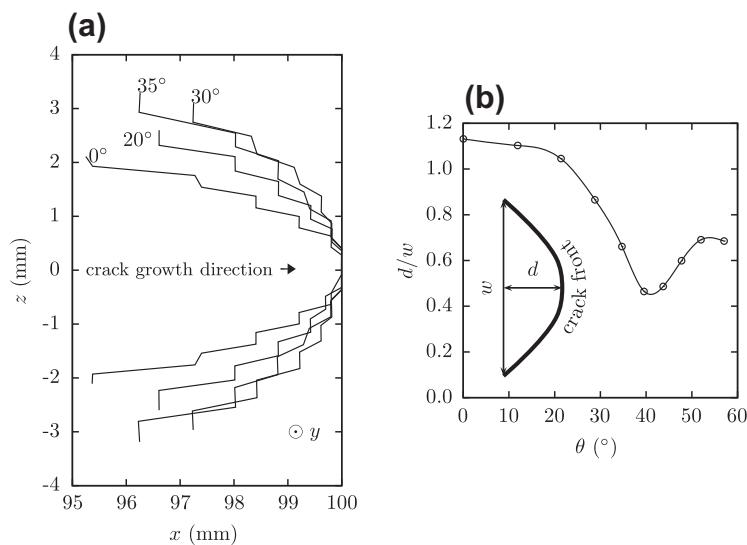


Fig. 12. (a) Crack front in the x – z plane for various initial tilt angles. (b) Crack aspect ratio as a function of the final tilt angle.

4.5. Comparison with experimental results and trends

In this section, results of the simulations are compared with experimental trends reported in Section 2.

Load–displacement curve: Load–displacement curves plotted in Fig. 6b do not depend on the initial tilt angle up to the load maximum which is equal to 194 kN. Experimental maximum forces are about 150 kN (Fig. 3b). This difference can partially be explained by the fact that the plastic anisotropy of the material was not accounted for. Preliminary calculations using the anisotropic plasticity model published in Tanguy et al. [32] and keeping the same tensile response along the T direction lead to a maximum force equal to 180 kN which still overestimates the actual one. The maximum load also depends on the cell size h . Reducing h would further decrease the maximum load. Similar results would be obtained by increasing q_1 or q_2 . It is also important to keep in mind that the present FE model does not exactly represent the experimental setup as stated above. In particular it can be observed that holes machined in the MDCB specimen were plastically deformed during the experiments. The displacement imposed on the specimens to carry out the simulations should not be compared with the experimental displacement (Fig. 3b) which corresponds to the whole testing machine displacement.

Crack path: One expects the crack to follow the path for which the rate of energy dissipation R is minimum. In all simulated cases reported in this study, the minimum dissipated energy is obtained for a slant crack path with a tilt angle equal to 45° . This result agrees well with experimental results. However in some cases (see e.g. Fig. 3a) a V-shape crack path can be observed although the resulting energy dissipation rate is higher (note that it is also higher than for pure flat fracture as shown in Fig. 8). In this case the tilt angle is also close to 45° . This could result from the fact that two slanted crack paths can in fact be formed at either $+45^\circ$ or -45° from the loading direction. These two competing paths may lead to the formation of a V-shaped crack.

Local strains: Grids painted on the gage section confirm that strain along the crack propagation direction is very close to 0 in the steady state propagation region. The numerical axial deformation over a 20 mm gage section is equal to 16% for the case where R is minimum ($\theta_0 = 32^\circ$). The value is close to the experimental one (19%). Once again this slight discrepancy could be explained by the fact that plastic anisotropy was not accounted for. The initial tilt angle leading to the minimum dissipation is equal to 32° which lies within the experimental range (27° – 37°) which is however rather large.

CTOA: The minimum value of the CTOA which corresponds to a final tilt angle equal to 45° is equal to 7.6° (Fig. 11). It lies within the experimental range ($8.5^\circ \pm 2$). Note that the variations of the simulated CTOA for a final tilt angle between 0° and 50° are relatively small (1.3°) compared to the experimental scatter.

5. Parametric study

The numerical tool presented above can be used to study the effect of material model parameters on crack advance and crack path. In the following the effect of work hardening and the effect of secondary nucleation are investigated.

5.1. Effect of work hardening

In this section the hardening behavior of the material was assumed to follow a simple Ramberg–Osgood law expressed as (for uniaxial loading):

$$\varepsilon = \begin{cases} \frac{\sigma}{E} & \text{if } \sigma < \sigma_N \\ \frac{\sigma_N}{E} \left(\frac{\sigma}{\sigma_N} \right)^N & \text{otherwise} \end{cases} \quad (11)$$

where σ_N is the yield stress and N the hardening exponent. The various damage parameters were kept constant. Note that the GTN parameters q_1 and q_2 may depend on both N and σ_N/E as shown in [44]. Calculations were performed with $\sigma_N = 700$ MPa, $E = 210$ GPa and N between 5 (high hardening rate) and $+\infty$ (perfectly plastic behavior) The energy dissipation rate R is plotted as a function of the final tilt angle in Fig. 13a for various values of N . It is shown that R strongly increases with decreasing values of N . Whatever the value of N , R reaches a minimum value for $\theta \approx 45^\circ$. It is also interesting to consider the evolution of R normalized with respect to its value for flat fracture (referred to as R_0 hereafter). Results are shown in Fig. 13b. The relative decrease of R for $\theta \approx 45^\circ$ is much higher (up to 50%) for low hardening materials (i.e. high values for N) than for high hardening materials (about 10% for $N = 5$).

The minimum value of the dissipation rate (R^{\min}) together with R_0 are plotted as a function of the inverse of the hardening modulus ($1/N$) in Fig. 14a. Both are almost linear functions of $1/N$. The CTOA value corresponding to the minimum value of R (referred to as CTOA^{\min}) is plotted as a function of $1/N$ in Fig. 14-b. It is an increasing function of $1/N$ and correlates well with R^{\min} . Similar trends are obtained considering the average plastic deformation along the crack path $\langle p \rangle_{\text{slice}}$.

These results are consistent with experimental results published in the literature. The fact that the relative decrease of R with the tilt angle is small for materials with high work hardening can explain why these materials preferentially exhibit flat fracture. High speed testing results in adiabatic heating leading to low strain hardening or softening. The present results

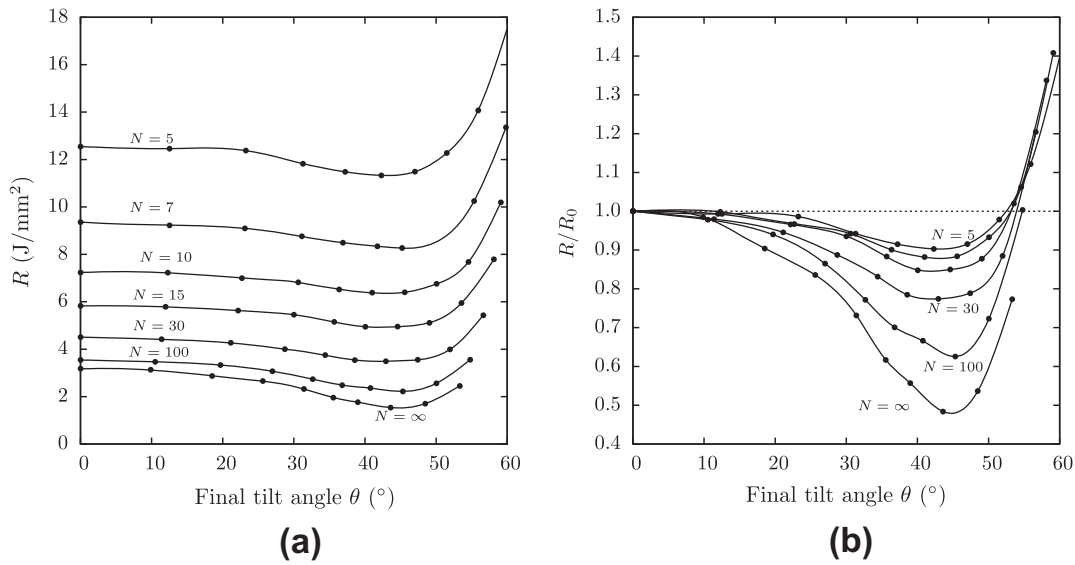


Fig. 13. (a) Dissipated energy as a function of the final tilt angle for various hardening exponents. (b) Normalized dissipated energy as a function of the final tilt angle for various hardening exponents.

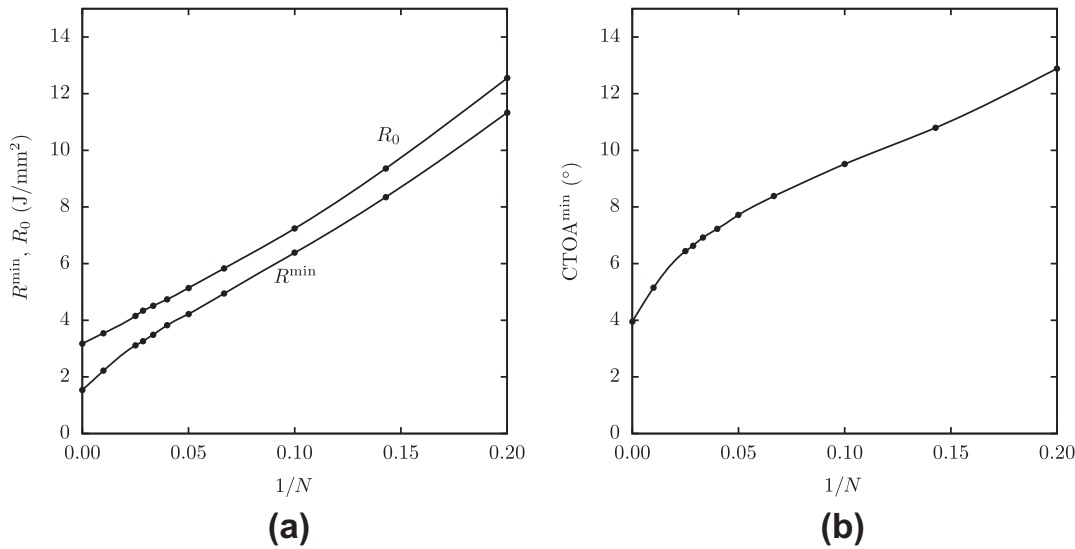


Fig. 14. (a) Minimum dissipation rate and dissipation rate for $\theta = \theta_0$ as a function of the inverse of the hardening modulus. (b) CTOA corresponding to the minimum dissipation rate as a function of the inverse of the hardening modulus.

explain why materials exhibiting pure flat fracture under quasi-static loading may exhibit slant fracture when tested under dynamic conditions.

5.2. Effect of secondary void nucleation

In general terms, shear is thought to play a major role for the flat to slant transition and for ductile fracture. It was shown by Wierzbicki and coworkers [45,46] that ductility may be reduced at a fixed stress triaxiality ratio in cases where the stress Lode parameter Λ is close to 0. For incompressible isotropic (von Mises plasticity) this state coincides with a plane strain state. Within the GTN framework, it was proposed by Nahshon and Hutchinson [47] to add a term in the damage evolution law (Eq. (6)) to represent this effect. This term can be interpreted as strain controlled nucleation with a nucleation rate parameter, A_n , depending on the stress Lode parameter which is maximum for $\Lambda = 0$ [23]. Noting that strain localization and subsequent formation of narrow bands in which additional damage can be nucleated is favored by plane strain conditions [42], it was proposed by [23] to use a nucleation term depending on the Lode parameter of the plastic strain rate tensor. This solution is similar to the one for which a dependence on the stress Lode parameter is chosen in the case of isotropic materials but different in the case of anisotropic plasticity often observed in the case of high grade line pipe steels.

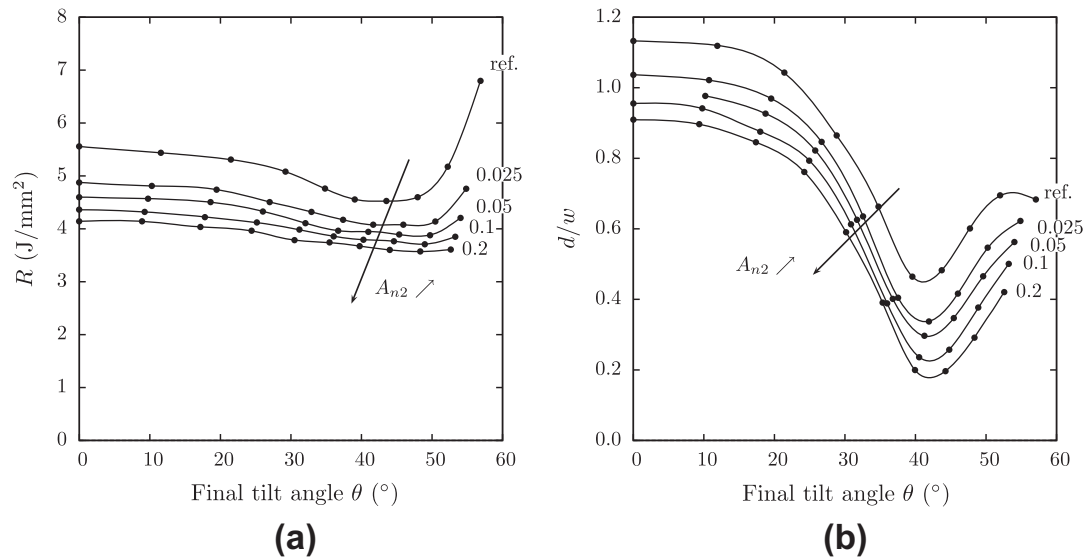


Fig. 15. Effect of the nucleation of additional voids (role of A_{n2}). (a) R as a function of the final tilt angle and (b) crack front aspect ratio a function of the final tilt angle.

Nucleation of a second void population may also be related to low stress triaxiality (i.e. less than 1.) failure. In that case very high plastic strain levels are reached so that new voids are nucleated on strengthening particles such as dispersoids in aluminum alloys [3] or iron carbides in steels [32]. Adding the description of such damage mechanisms within the GTN model framework is a way to extend the model to low stress triaxiality failure as the original model essentially deals with failure due to void growth.

In order to simply study the effect of secondary void nucleation in the steady state propagation regime, it is assumed that additional voids can be nucleated following a strain controlled nucleation kinetics expressed as:

$$\dot{f}_{n2} = \begin{cases} 0 & \text{if } p < p_{c2} \\ A_{n2}\dot{p} & \text{otherwise} \end{cases} \quad (12)$$

The description of secondary nucleation introduces two new material parameters A_{n2} and p_{c2} . All other material parameters are kept constant (see Table 1). In Fig. 15a the energy dissipation rate is plotted as a function of the final tilt angle for $p_{c2} = 0.5$ for various values for the nucleation rate $A_{n2} = 0 \dots 0.2$. The relatively high value of p_{c2} is such that the second nucleation mechanism is not activated at high stress triaxiality. R is a decreasing function of A_{n2} and the minimum value is still

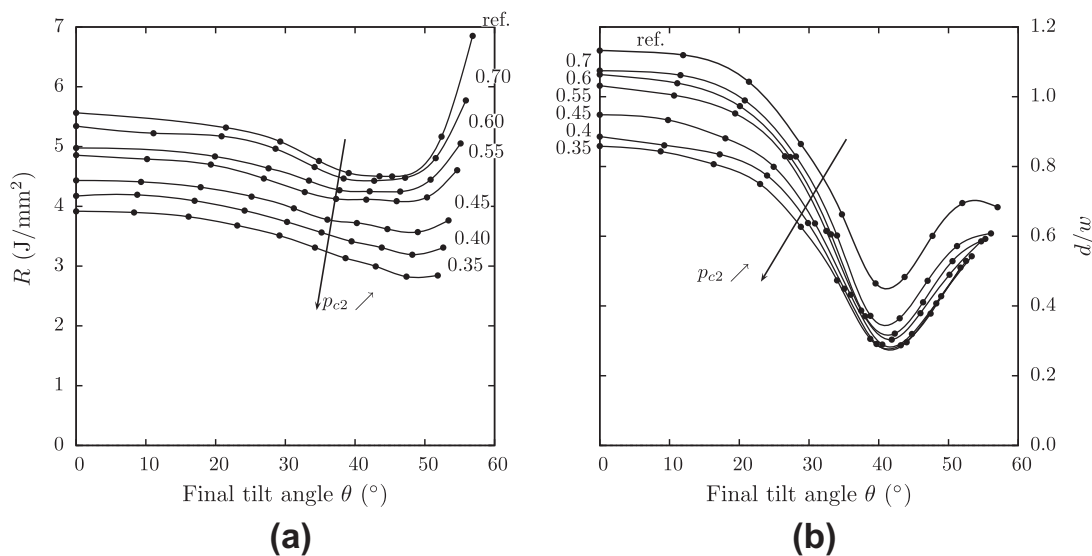


Fig. 16. Effect of the nucleation of additional voids (role of p_{c2}). (a) R as a function of the final tilt angle and (b) crack front aspect ratio a function of the final tilt angle.

obtained for $\theta \approx 45^\circ$. Similar variations are obtained for the CTOA. The crack front aspect ratio d/w is plotted in Fig. 15b. Values as low as 0.2 (i.e. almost straight crack front) can be obtained for $\theta \approx 45^\circ$. Similar trends are obtained when varying the critical plastic strain for secondary nucleation p_{c2} (see Fig. 16) for a fixed value of A_{n2} equal to 0.05.

These results show that a further reduction in energy dissipation rate (or CTOA or mean plastic strain) may result from additional damage occurring during the steady state crack growth due to the local stress/strain state prevailing in this region. However it does not appear to be necessary to add these terms to predict a minimum value for R when the crack is tilted at 45° . This is in contradiction with results of Xue and Wierzbicki [22] and Morgeneyer and Besson [23] who showed that additional Lode parameter dependent damage was required to simulate slant fracture. Two possible explanations for this discrepancy can be proposed: (i) the meshes were too coarse to allow flat to slant transition without additional damage and (ii) additional damage plays a crucial role in the flat to slant transition region where the crack has to deviate from its original plane.

6. Conclusions

The stable tearing behavior of a pipeline steel (X100 grade) was numerically investigated using the computational cell technique in the case of a modified double cantilever beam. The computational cell technique allows simulating slant crack advance for various crack tilt angles. The dependence of crack growth parameters (energy dissipation rate, CTOA, mean plastic strain) on the tilt angle was systematically investigated using this technique. A simple GTN model was used to simulate ductile damage growth within the computational cells. The main results are summarized as follows:

- The energy dissipation rate R reaches a minimum value in the case of S-shape slant fracture for a final tilt angle equal to 45° . This result is consistently obtained whatever the hypotheses made on the material hardening or damage parameters. Such a minimum value is not obtained in the case of V-shape fracture. This result explained why slant fracture is often observed during ductile tearing in thin sheets. V-shape fracture may occur due the existence of two possible slanted crack paths.
- The energy dissipation rate correlates well with CTOA values and the mean plastic strain along the crack path.
- Stress and strain states in the stable tearing region hardly depend on the assumed tilt angle. In this region, values of the stress triaxiality ratio (and damage growth rate) are lower than in the initial flat triangular region. The Lode parameter is close to 0 and tearing occurs under plane strain along the crack growth direction. Both of these conditions tend to favor strain localization within a band making an angle with the loading direction equal to 45° .
- Simulations indicate that the CTOA on the surface of the specimen is close to the CTOA at the center of the specimen (steady state propagation).
- When the work hardening rate is increased, R still reaches a minimum value for a tilt angle equal to 45° . However, the relative difference between this minimum and the value corresponding to flat fracture is reduced so that flat fracture prevails for materials with a high work hardening rate.
- The deformation state (plane strain) and stress state (Lode parameter close to zero) are thought to cause additional damage [22,47] besides the fact that they promote localization. This can be represented by additional damage nucleation in the stable tearing region. In that case, the above conclusions are still valid and fracture parameters such as energy dissipation rate, CTOA or mean plastic strain are reduced.
- The present study was carried out assuming plastic isotropy for the sake of simplicity whereas the actual behavior of grade X100 steels is anisotropic [32]. Accounting for plastic anisotropy in the calculations is not expected to modify the main findings of the present study. Flat to slant transition will correspond to a similar change in stress state and the slanted crack will still propagate under plane strain conditions for which the localization angle is 45° .

Acknowledgement

The work by JB was supported by the industry chair “Durability of materials and structures for energy” supported by EDF and GDF-SUEZ/GRT Gaz at Mines ParisTech and Ponts ParisTech.

References

- [1] Xia L, Shih CF. Ductile crack growth – I. A numerical study using computational cells with microstructurally-based length scales. *J Mech Phys Solids* 1995;43:233–59.
- [2] Mahgoub E, Deng X, Sutton M. Three-dimensional stress and deformation fields around flat and slant cracks under remote Mode I loading conditions. *Engng Fract Mech* 2003;70:2527–42.
- [3] Bron F, Besson J, Pineau A. Ductile rupture in thin sheets of two grades of 2024 aluminum alloy. *Mater Sci Engng A* 2004;380:356–64.
- [4] Asserin-Lebert A, Besson J, Gourgues A-F. Fracture of 6056 aluminum sheet materials: effect of specimen thickness and hardening behavior on strain localization and toughness. *Mater Sci Engng A* 2005;395:186–94.
- [5] Lan W, Deng X, Sutton M, Cheng C-S. Study of slant fracture in ductile materials. *Int J Fract* 2006;141(3–4):469–96.
- [6] Morgeneyer TF, Helfen L, Sinclair I, Proudhon H, Xu F, Baumbach T. Ductile crack initiation and propagation assessed via in situ synchrotron radiation-computed laminography. *Scr Mater* 2011;65(11):1010–3.

- [7] Shterenlikht A, Hashemi S, Howard I, Yates J, Andrews R. A specimen for studying the resistance to ductile crack propagation in pipes. *Engng Fract Mech* 2004;71:1887–2013.
- [8] Rivalin F, Pineau A, Di Fant M, Besson J. Ductile tearing of pipeline-steel wide plates – I. Dynamic and quasi-static experiments. *Engng Fract Mech* 2000;68(3):329–45.
- [9] Pardoën T, Marchal Y, Delannay F. Essential work of fracture compared to fracture mechanics – towards a thickness independent plane stress toughness. *Engng Fract Mech* 2002;69:617–31.
- [10] Pardoën T, Hachez F, Marchioni B, Blyth P, Atkins A. Mode I fracture of sheet metal. *J Mech Phys Solids* 2004;52(2):423–52.
- [11] Hara T, Shinohara Y, Terada Y, Asahi H. DWTT properties for high strength line pipe steels. In: Proc. Eighteenth Int. Offshore and Polar Engineering Conf., Vancouver, Canada, ISOPE; 2008. p. 189–93.
- [12] Gurson AL. Continuum theory of ductile rupture by void nucleation and growth: Part I – Yield criteria and flow rules for porous ductile media. *J Engng Mater Technol* 1977;99:2–15.
- [13] Tvergaard V, Needleman A. Analysis of the cup-cone fracture in a round tensile bar. *Acta Metall* 1984;32:157–69.
- [14] Besson J, Steglich D, Brocks W. Modeling of crack growth in round bars and plane strain specimens. *Int J Solids Struct* 2001;38(46–47):8259–84.
- [15] Besson J, Steglich D, Brocks W. Modeling of plane strain ductile rupture. *Int J Plast* 2003;19(10):1517–41.
- [16] Huespe AE, Needleman A, Oliver J, Sánchez PJ. A finite thickness band method for ductile fracture analysis. *Int J Plast* 2009;25(12):2349–65.
- [17] Huespe AE, Needleman A, Oliver J, Sanchez PJ, strain A finite. finite band method for modeling ductile fracture. *Int J Plast* 2012;28(1):53–69.
- [18] Scheider I, Brocks W. Simulation of cup-cone fracture using the cohesive model. *Engng Fract Mech* 2003;70(14):1943–61.
- [19] Mathur K, Needleman A, Tvergaard V. Three dimensional analysis of dynamic ductile crack growth in a thin plate. *J Mech Phys Solids* 1996;44(3):439–64.
- [20] Besson J, Brocks W, Chabanet O, Steglich D. Ductile rupture of aluminum sheet materials. *Eur J Finite Elem* 2001;10:401–15.
- [21] Xue L, Wierzbicki T. Ductile fracture initiation and propagation modeling using damage plasticity theory. *Engng Fract Mech* 2008;75(11):3276–93.
- [22] Xue L, Wierzbicki T. Numerical simulation of fracture mode transition in ductile plates. *Int J Solids Struct* 2009;49:1423–35.
- [23] Morgeneyer TF, Besson J. Flat to slant ductile fracture transition: tomography examination and simulations using shear-controlled void nucleation. *Scripta Metall Mater* 2011;65:1002–5.
- [24] Xia L, Shih CF, Hutchinson JW. A computational approach to ductile crack growth under large scale yielding conditions. *J Mech Phys Solids* 1995;43(3):389–413.
- [25] Ruggieri C, Panontin T, Dodds Jr RH. Numerical modeling of ductile crack growth in 3-d using computational cell elements. *Int J Fract* 1996;82:67–95.
- [26] Gullerud AS, Dodds RH, Hampton RW, Dawicke DS. Three dimensional modeling of ductile crack growth in thin sheet metals: computational aspects and validation. *Engng Fract Mech* 1999;63:347–73.
- [27] Gullerud AS, Gao X, Dodds Jr RH, Haj-Ali R. Simulation of ductile crack growth using computational cells: numerical aspects. *Engng Fract Mech* 2000;66:65–92.
- [28] Qian X. An out-of-plane length scale for ductile crack extensions in 3-D SSY models for X65 pipeline materials. *Int J Fract* 2011;167:249–65.
- [29] Siegmund T, Brocks W. Prediction of the work of separation and implications to modelling. *Int J Fract* 1999;99:97–116.
- [30] Herynk MD, Kyriakides S, Onoufriou A, Yun HD. Effects of the UOE/UOC pipe manufacturing processes on pipe collapse pressure. *Int J Mech Sci* 2007;49(5):533–53.
- [31] Shinohara Y, Madi Y, Besson J. A combined phenomenological model for the representation of anisotropic hardening behavior in high strength steel line pipes. *Eur J Mech/A* 2010;29(6):917–27.
- [32] Tanguy B, Luu T, Perrin G, Pineau A, Besson J. Plastic and damage behavior of a high strength X100 pipeline steel: experiments and modelling. *Int J Press Vess Pip* 2008;85(5):322–35.
- [33] Darcis P, McCowan C, Windhoff H, McColskey J, Siewert T. Crack tip opening angle optical measurement methods in five pipeline steels. *Engng Fract Mech* 2008;75:2453–68.
- [34] Sowards J, McCowan C, Drexler E. Interpretation and significance of reverse chevron-shaped markings on fracture surfaces of API X100 pipeline steels. *Mater Sci Engng A* 2012;551:140.
- [35] Tvergaard V. Material failure by void growth to coalescence. *Adv Appl Mech* 1990;27:83–151.
- [36] Chu C, Needleman A. Void nucleation effects in biaxially stretched sheets. *J Engng Mater Technol* 1980;102:249–56.
- [37] Besson J, Foerch R. Large scale object-oriented finite element code design. *Comput Meth Appl Mech Engng* 1997;142:165–87.
- [38] Foerch R, Besson J, Cailletaud G, Pilvin P. Polymorphic constitutive equations in finite element codes. *Comput Meth Appl Mech Engng* 1997;141:355–72.
- [39] Sidoroff F, Dogui A. Some issues about anisotropic elastic–plastic models at finite strain. *Int J Solids Struct* 2001;38:9569–78.
- [40] Hughes T. Generalization of selective integration procedures to anisotropic and nonlinear media. *Int J Numer Meth Engng* 1980;15:1413–8.
- [41] Bron F, Besson J. Simulation of the ductile tearing for two grades of 2024 aluminum alloy thin sheets. *Engng Fract Mech* 2006;73:1531–52.
- [42] Needleman A, Rice J. Limits to ductility set by plastic flow localization. In: Koistinen EDP, editor. *Mechanics of Sheet Metal Forming*. Plenum Publishing Corporation; 1978. p. 237–67.
- [43] Lan W, Deng X, Sutton M. Investigation of crack tunneling in ductile materials. *Engng Fract Mech* 2010;77(14):2800–12.
- [44] Faleskog J, Gao X, Shih C. Cell model for nonlinear fracture analysis – I. Micromechanics calibration. *Int J Fract* 1998;89:355–73.
- [45] Bai Y, Wierzbicki T. A new model of metal plasticity and fracture with pressure and Lode dependence. *Int J Plast* 2008;24(6):1071–96.
- [46] Bai Y, Wierzbicki T. Application of extended Mohr–Coulomb criterion to ductile fracture. *Int J Fract* 2010;161(1):1–20.
- [47] Nahshon K, Hutchinson J. Modification of the Gurson model for shear failure. *Eur J Mech/A* 2008;27A:1–17.